

Research Article

Postprocessing Study for the Controllable Structures of Ceramic Green Parts Realized by a Flexible Binder Jetting Printing (BJP) Solution

Shu Cao ¹, Fangxia Xie,¹ Xueming He,² Chaofeng Zhang ¹ and Meiping Wu²

¹School of Mechanical Engineering, Jiangnan University, Wuxi 214122, Jiangsu, China

²Key Laboratory of Advanced Food Manufacturing Equipment and Technology, Wuxi 214122, Jiangsu, China

Correspondence should be addressed to Shu Cao; caoshumse@jiangnan.edu.cn

Received 2 November 2019; Accepted 16 December 2019; Published 8 January 2020

Academic Editor: Tomasz Trzepieciński

Copyright © 2020 Shu Cao et al. This is an open access article distributed under the Creative Commons Attribution License, which permits unrestricted use, distribution, and reproduction in any medium, provided the original work is properly cited.

For indirect ceramic additive manufacturing (AM), green parts' initial densities are low, limiting the postprocessing strengthening under atmospheric pressure. This study employed binder jetting printing (BJP) based on the polycondensation curing of urea-formaldehyde resin to produce series of Al_2O_3 green specimens with controllable structures. Further, an integrated postprocessing procedure, including the sequential stages of presintering, ceramic slurry infiltration, and final sintering, was conducted on these green specimens with designed structural characteristics for verifying strengthening mechanism. Using a self-developed BJP machine system and the related material which are flexible in process, this study printed green specimens with strong bonding (flexural strength above 6.84 MPa), additionally can regulate their initial densities within the wide range between 21.7%~43.9%. Infiltrated with ceramic slurry, low-density green specimens were significantly strengthened via final sintering, realizing final densities, flexural strength, and compressive strength of 73.2%, 43.15 MPa, and 331.17 MPa, respectively. In comparison, high-density specimens performing poor infiltration obtained limited density increment after final sintering, but better mechanical properties and surface strengthening were realized, exhibiting final densities, flexural strength, comprehensive strength, surface roughness R_a , and Vickers hardness of 70.1%, 63.22 MPa, 450.18 MPa, 9.73 μm , and 4.58 GPa, respectively. In summary, this study is helpful to provide the technical reference for custom AM ceramic green parts and the postprocessing optimization.

1. Introduction

Various advantages of wear resistance, high-temperature performances, anticorrosion character, and light weight make ceramics the ideal structural bulk material in extreme engineering conditions [1]. However, production of ceramics mostly relies on mold forming, bringing about the economic and time-consuming problems as well as the difficulty in realizing intricate shapes [2]. Current mold-based ceramic production, suitable for medium or large-scale manufacturing, is not in line with the future trend of small-batch customization [3]. Over more than 20-year development, additive manufacturing (AM), capable of forming arbitrary-shaped parts [4], offers a new path to rapid production of complex-shaped ceramic green parts.

Nevertheless, the AM for ceramics is still far behind the mature solutions for metals and polymers [5].

Presently, ceramic AM is mainly divided into a direct and an indirect way. The direct way is completed using high-power source, e.g., the laser beam, to in situ sinter the ceramic powder to form final ceramic products and simultaneously achieve part strength [6]. The indirect way first forms ceramic green parts via powder-bonding methods at room temperature or with low-power energy, followed by postprocessing, to guarantee the final ceramic products with strengthened performances [7–11]. Generally, only specific ceramic-based material systems are suitable for direct-way production due to the high melting point of ceramic components, so the indirect way is still the mainstream for ceramic AM [12].

Indirect ceramic AM hardly realizes high-density ceramic green parts [13]. Thus, it is difficult to offer the ceramic green parts with sufficient strength via conventional postprocessing, restricting the further engineering applications. A stereo-lithography (SL) process can significantly increase the densities of the green parts by preparing the ceramic-based photocurable resin with very high solid loadings. However, the resin preparation is complicated as it is necessary to control the rheological behavior and restrain the scattering of UV laser resulting from the embedded ceramic particles [14]. Besides, extrusion free forming (EFF) also needs to tailor the rheological properties of the high solid-loading ceramic slurry [15]. In contrast, binder jetting printing (BJP) and selective laser sintering (SLS) use dry ceramic powder material, so the material preparation is convenient. Additionally, optimizing the size distribution of powder particles can facilitate the powder packing within the green parts [16]. The densification can also be improved by decreasing the layer thickness during powder dispensing [17]. Introducing vibration excitation during powder dispensing is also beneficial to promote powder flow to form a denser powder bed [18]. Moreover, the green parts can also be isostatically pressed to substantially reduce the pores, which remarkably increases the part's densification [19] but is only suitable for the simple-shaped preforms. However, the above strategies provide these dry-powder-formed green parts with very limited densification improvement except for the isostatic pressing which is very effective but also tends to cause large distortions. Generally, the density of the dispensed powder bed is only 70% of the tap density of powder material [14]; in addition, the binders are often involved within the powder material. After binder pyrolysis, the debinded structures in the form of ceramic matrix usually have the relative densities below 30%.

According to above reasons, increasing the initial densities of green parts and strengthening them through atmospheric-pressure postprocessing procedure with moderate volume shrinkages are very important to the economical AM of high-performance bulk ceramic. Slurry-based infiltration of submicron ceramic particles into the ceramic green parts can directly increase the density, and after the follow-up sintering, the ceramic products are expected to achieve excellent performances. At present, ceramic slurry infiltration has been generally proved to be effective in improving the structural and mechanical properties of the AM ceramic products. Related investigations have focused on the factors of infiltration pressure, solid loadings of slurry, and preform dimensions influencing on the infiltration effects [12, 20–23]. Besides the above influencing factors, the infiltration behaviors of ceramic slurry are greatly affected by the factors of the part microstructures. As a result, AM ceramic green parts with different initial structural characteristics might experience different infiltration process, and the related infiltration mechanism is supposed to be verified. To our knowledge, the related publications have been seldom presented.

Based on the curing mechanism of urea-formaldehyde (UF) polycondensation, an in-house developed BJP solution including a machine system and own material, capable of

flexible process setups, was adopted to print Al_2O_3 green specimens having initial densities within a controllable wide range. Afterwards, densification conditions, mechanical strengths, and microstructure evolutions of these specimens were characterized and analyzed within an integrated postprocessing procedure, including the sequential stages of presintering, ceramic slurry infiltration, and final sintering. Moreover, the behavior of ceramic slurry penetrating into the specimens with diverse structural conditions and the resultant strengthening effects were emphasized. This study included details in tailoring ceramic green specimens with designed structural characteristics by BJP additive manufacturing process and also investigated the strengthening mechanism influenced by these structural factors during an integrated postprocessing procedure, reflecting good scientific significances for giving postprocessing advices to the AM ceramic green parts formed under different conditions.

2. Materials and Methods

2.1. Material Preparation. In the past, the binders of sols or organic adhesive were placed within the printing liquid to improve the bonding effects for BJP process. However, in-liquid binders are prone to precipitate insoluble matters, causing nozzle blockage. Accordingly, the in-powder binder as an alternative strategy is commonly used at present. For ensuring the adequate bonding, the ratios of binder in powder material should be large and thorough homogenization is required. It is disadvantageous that the in-powder binder, as a sacrificial component, will be removed in postprocessing and more pores are generated within structures. As a result, plenty use of in-powder binder will inevitably reduce the part densification, revealing a kind of “pore-forming” effect. This study used powdered UF resin as binder to reduce the binder usage and meanwhile simplify the material preparation.

Powdered UF resin is very soluble in water, and the solution can be cured by the polycondensation reaction which is easily activated in the weak acid environment to achieve strong bonding [24]. Thereby, the powdered UF can be combined with ceramic powder to conveniently prepare the ceramic BJP powder material, while the printing liquid can be also simplified to a weakly acidic aqueous solution free of binder.

Considering that in-powder binder leads to the aforementioned “pore-forming” effect on the part structures, two types of Al_2O_3 -based powder material with different UF ratios were prepared in this study in order to produce the ceramic green specimens with varied initial structural characteristics within a wider range. The formulations are shown in Table 1. The raw components of each type of powder material were put into a high-speed blender. Then, the mixture was mechanically uniformized for about 30 min; meanwhile, the blending process was paused every interval of 2 min to protect the blender motor. After this convenient uniformization, two types of as-prepared powder material were naturally cooled for use, their particle size distributions were measured using laser granulometer (Mastersizer 2000,

TABLE 1: Two sets of formulations for powder material with different UF contents.

Raw powder component	Weight ratios	
	Type-A powder	Type-B powder
Al ₂ O ₃ powder #1 ($D_{50} = 45.81 \mu\text{m}$)	68.5	63.0
Al ₂ O ₃ powder #2 ($D_{50} = 5.73 \mu\text{m}$)	24.3	22.7
UF powder ($D_{50} = 0.59 \mu\text{m}$)	7.2	14.3

Malvern Instruments, UK), and their microscopic morphologies were examined by scanning electron microscopy (SEM, Nova 630, FEI Company, USA). For each type of powder material, using two groups of Al₂O₃ components is for increasing the powder packing owing to the particle size differences [16]. Note that the homogenization was realized just by mechanical blending and Type-A powder material only contained UF binder with very low ratio of 7.2 wt%. However, the following experiments will prove the BJP solution is suitable to produce ceramic green parts with high bonding strength.

The printing liquid was conveniently prepared as follows: NH₄Cl as the curing agent (i.e., pH regulator) together with the additives (including humectant, flow modifier, and preservative) were dissolved in deionized water; afterwards, the mixture was magnetically stirred for 2 h to complete the preparation of the printing liquid of weakly acid aqueous solution. The formulation of the printing liquid is shown in Table 2. Before use, the printing liquid further required the deforming process under vacuum. The viscosity, surface tension, and pH value of the prepared printing liquid were further determined in order to demonstrate its printability and its reaction capability with UF.

2.2. Self-Developed BJP System. The adoption of weakly acidic printing liquid free of binder eases the selection of printhead for an in-house developed BJP system. A low-cost piezoelectric printhead (ME series, EPSON, Japan) originally applied to a desktop inkjet printer was integrated onto the BJP system. The fast-axis scanning motion of printhead was realized by the original control board of the desktop printer, whereas the slow-axis step motion was achieved by the synergistic control with the linkage of fast-axis motion signals detected and processed by a customized circuit. Additionally, the usage of this desktop printhead makes it easy to adjust the printing liquid saturation by activating different numbers of nozzles through printing color settings. Besides the printing unit, the BJP system consists of a powder-layering unit and a platform-elevating unit, respectively, for dispensing powder layers and precisely controlling the powder layer thickness, as shown in Figure 1.

As for layering powder by the conventional counter-rolling (CR) method, a roller traverses over the powder bed and rotates against the traversing direction, leveling the powder pile to dispense intact powder layer. In comparison, the double-smoothing (DS) method dispenses one powder layer with two rounds of CR powder layering as shown in Figure 2, enabling the dispensed powder layers with reduced

TABLE 2: Formulation for weakly acidic aqueous printing material.

Ingredient	Composition	Ratios (wt%)
Solvent	Distilled water	85.2
Humectant	Glycerol	5.0
Flow modifier	Isopropanol	0.6
Curing agent (pH regulator)	NH ₄ Cl	9.0
Preservative	Potassium sorbate	0.2

surface defects and more importantly improving the powder densification according to the previous work [25]. Assisted with flexible adjustment of powder layer thickness which also influences powder packing [17], the self-developed BJP system switched between the CR method and DS method, realizing the designated densification effects for the dispensed powder layers, i.e., for the printed ceramic green parts.

The platform-elevating unit incorporated a worm-gear reducer within the transmission chain. As a result, the platform supporting the powder bed moved more reliably, and most importantly, the elevating motion precision could be enhanced owing to the large reduction ratio of reducer.

2.3. Printing Al₂O₃ Green Specimens. The commercial BJP system and its specialized material restrict the flexibility during BJP process, resulting in a printed green part with relatively constant structural characteristics, which is not pertinent to the following discussion of the structural influences during postprocessing in this study. The in-house developed BJP system and own material allow the flexible process setups, such as adjustments of powder-layering method, the powder layer thickness, and the powder material compositions. As shown in Table 3, a series of experiment groups of green specimens were printed by the flexible BJP solution in this study, expected to designate initial green densities to specimens in different groups.

As multiple properties of the specimens were required to be characterized in the study, two types of compressive specimens (ASTM C1424-10 Standard) and flexural specimens (ISO 14704:2008 Standard) were printed for each experiment group in this study, as shown in Figure 3. Compressive specimens were specific for the compressive strength tests, while flexural specimens were specific for the flexural strength, densities, linear shrinkages, observation of microstructures, and other supplementary specimen properties. It should be mentioned that the specimen dimensions in Figure 3 were larger than those specified by above standard test methods. These size margins were designated to compensate for the volume shrinkages of the specimens caused by postprocessing and also for the grinding of specimens to reduce surface cracks before the tests for mechanical strength.

The printed Al₂O₃ green specimens were naturally dried within the powder bed for 1.5 h and dug out to cure at 110°C for 30 min in an oven. After curing, the flexural strength of printed specimens was measured by a universal testing machine (MTS810 MTS Systems, USA), the specimen

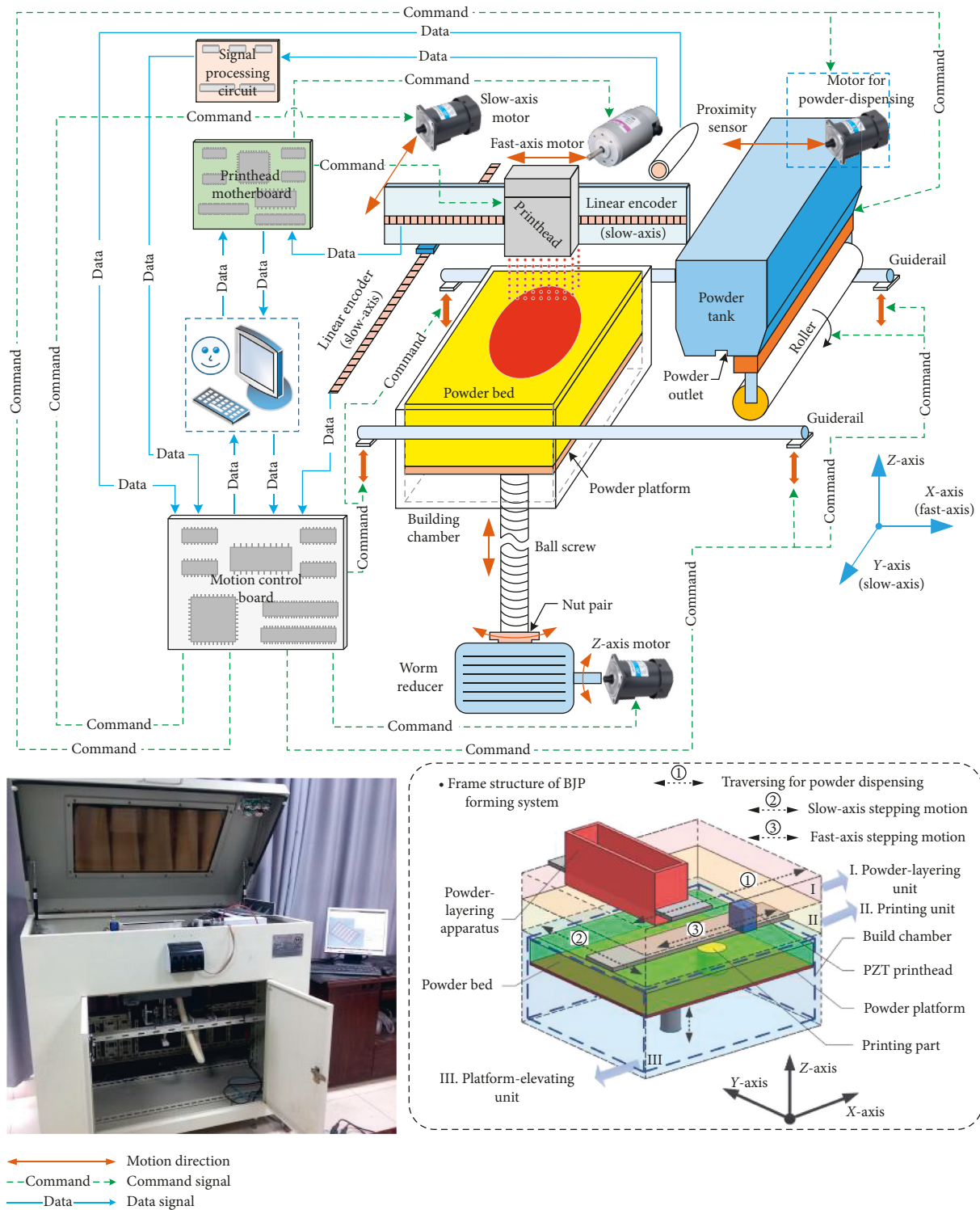


FIGURE 1: In-house developed BJP forming machine system.

microscopic morphologies were observed by SEM, and initial length of the strip-shaped flexural specimens was measured by a digital microscope (VHX-600E, Keyence, Japan). Considering the ceramic matrix in the printed specimens was full of cured binder component, the actual initial density would be measured after the debinding process.

2.4. *Debinding.* Effective pyrolysis of the binder component within the ceramic green specimens benefits the sinter strengthening. In this study, the high-temperature decomposition behaviors of the UF binder were characterized by thermogravimetric analysis (TGA, SDTA851, Mettler Toledo, Germany). The TGA results for the cured UF binder shown in Figure 4 indicate that

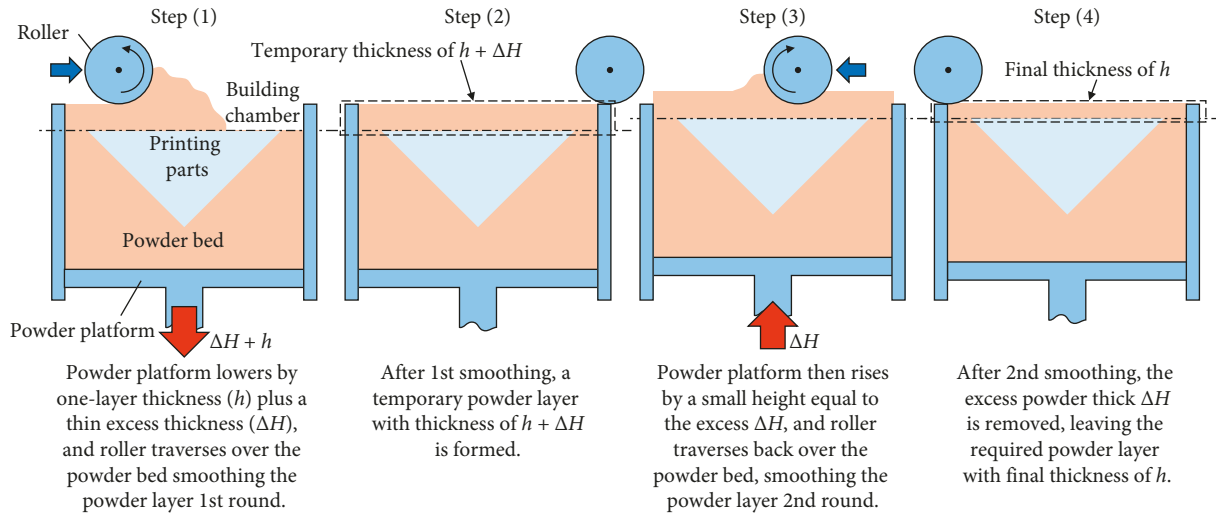


FIGURE 2: DS method (procedure for dispensing one powder layer with final thickness of h).

TABLE 3: Experiment groups and their corresponding process setups.

Group no.	Powder type	Layering method	Layer thickness h (μm)	Excess thickness ΔH (μm)
I	Powder B	CR	150	—
II	Powder B	CR	130	—
III	Powder B	CR	110	—
IV	Powder A	CR	150	—
V	Powder A	CR	130	—
VI	Powder A	CR	110	—
VII	Powder A	DS	150	80
VIII	Powder A	DS	130	80
IX	Powder A	DS	110	80

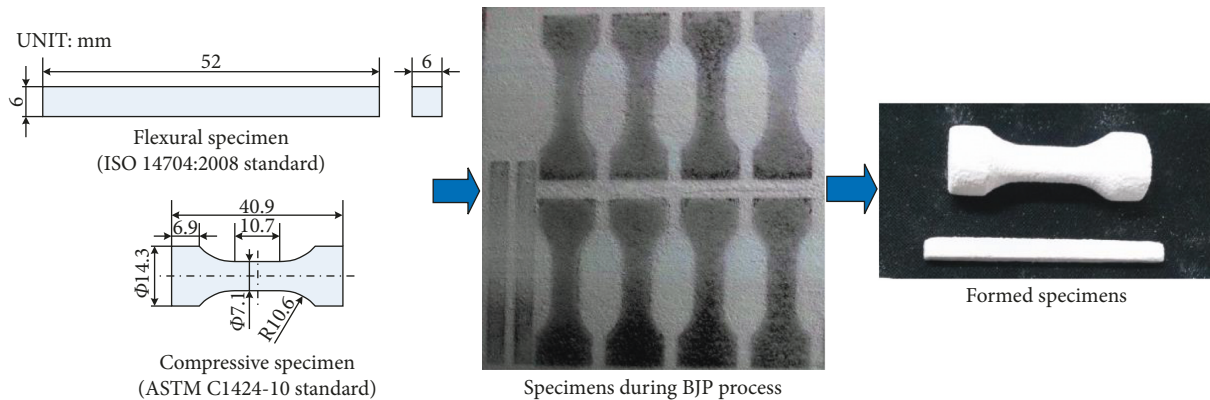


FIGURE 3: Two types of standard test specimens formed for each experiment group.

UF binder decomposed very efficiently in the temperature range of about 277°C ~ 358°C , and only a small residue was left at a temperature above 550°C , revealing UF as a good sacrificial binder for ceramic AM based on the BJP process. On the basis of these TGA results, the debinding temperature schedule is as shown in Figure 5. The debinding was mainly performed at the temperature of 350°C and 550°C for 1.5 h and 1 h, for increasing the UF pyrolysis rate and minimizing the UF residues, respectively.

After debinding, X-ray diffraction (XRD, Empyrean, PANalytical, the Netherlands) analysis was conducted on the specimens to verify the completeness of the pyrolysis of UF binder. At this stage, the initial densities of the green specimens were measured by the drainage method [25]. Also, the microstructures of the debinded specimens were evaluated by SEM.

2.5. Presintering. After debinding, the bonds between the Al_2O_3 particles in the specimens were almost eliminated. The

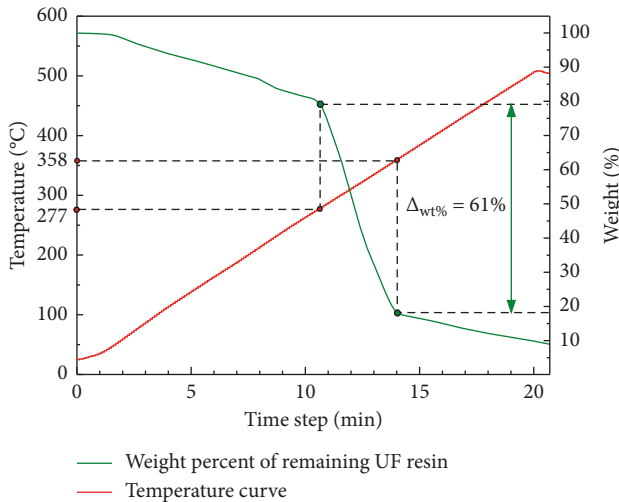


FIGURE 4: TGA results for the cured UF binder (between room temperature and 560°C).

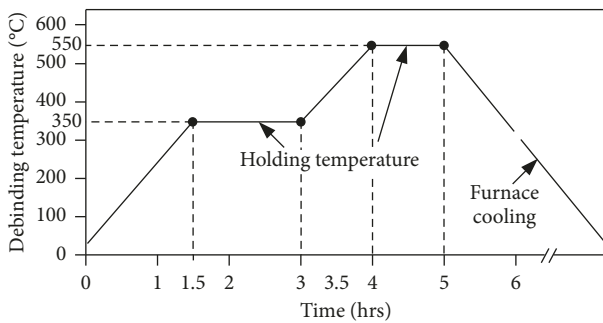


FIGURE 5: Temperature schedule for debinding process.

resultant discrete structure of ceramic matrix was required to be preliminarily strengthened by presintering in order to withstand the working pressure during the follow-up ceramic slurry infiltration. The temperature schedule for presintering is shown in Figure 6. Note that the specimens were not fully sintered at this stage, so presintering temperature of 1500°C for just 1.5 h was applied. After presintering, specimens were taken to the test of compressive strength, verifying whether they met the pressure requirements by the following infiltration. The presintered specimens were measured for their densities by the draining method, and their microstructures were observed by SEM.

2.6. Ceramic Slurry Preparation. Submicron α - Al_2O_3 particles ($D_{50} \approx 0.25 \mu\text{m}$, Nanuo chemistry&tech, China) in the form of slurry were required to infiltrate the presintered specimens for directly improving the densification of Al_2O_3 ceramic matrix. Ammonium polyacrylate was adopted as dispersant in this study. Its acidic unit can generate surface negative charges onto the Al_2O_3 submicron particles. The charge repulsion can substantially avoid particle agglomeration, reduce the slurry viscosity, and facilitate the infiltration. However, an excessive amount of dispersant must be avoided, as agglomeration of the particles would be

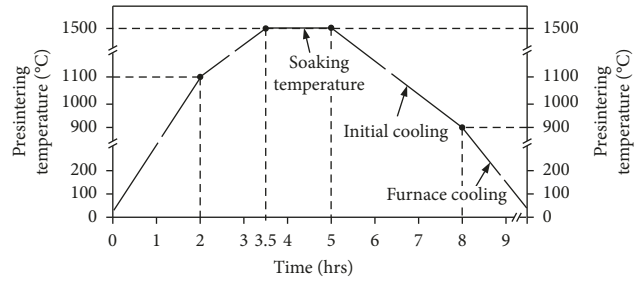


FIGURE 6: Temperature schedule for presintering process.

adversely induced by the bridging effect between the free ions [26]. For this reason, the formulation of the Al_2O_3 slurry was elaborately assessed by continuously adjusting the pH values and measuring the matching viscosities. The final compositions for two types of Al_2O_3 slurry with the solid loadings of 30 vol% and 40 vol% are shown in Table 4. The two types of slurry had viscosities of 0.87 Pa·s and 1.13 Pa·s, respectively. Note that before infiltration, the prepared slurries required a step of air-bubble elimination under vacuum.

2.7. Ceramic Slurry Infiltration. A home-made infiltration apparatus capable of two working modes of vacuum infiltration and pressure infiltration was adopted in this study. The related operation is shown in Figure 7.

Step (1). The specimen was put into a breaker which was full of ceramic slurry and placed inside a pressure tank, and then the tank cover and the all the gas lines on the tank were closed. Afterwards, the line connecting to vacuum pump was opened, pumping out the air inside the specimen.

Step (2). Once the vacuum within the pressure tank was stabilized, the line connected with atmosphere was opened after closing all the other lines again, and therewith, the resultant atmospheric pressure upon the ceramic slurry resulted in the penetration of slurry into the specimens (i.e., the vacuum infiltration).

Step (3). The compressed air line (with the gauge pressure up to 1 MPa) was opened with all the other lines sealed, then the pressure reducing valve was used to adjust the compressed air which entered the tank, and afterwards, the increased pressure upon the slurry additionally promoted the slurry penetration into the specimens (i.e., the pressure infiltration).

Step (4). For safety, while opening up tank cover in the case of pressure infiltration, the silencer must be opened in advance to slowly relieve pressure.

The aforementioned types of 30 vol% and 40 vol% Al_2O_3 slurry were applied to the infiltration investigation, and the specimens were infiltrated with varied gauge pressures of 0 MPa (i.e., vacuum infiltration), 0.2 MPa, 0.5 MPa, 0.8 MPa, and 1 MPa, respectively. After freeze-drying, the densities of the infiltrated specimens were determined by weighting, the infiltration effects inside the specimens were observed by

TABLE 4: Formulation of two ceramic slurries with different Al₂O₃ solid loads.

Slurry type	Distilled water	Al ₂ O ₃ micropowder	Polyvinyl alcohol	Glycerol	Ammonium polyacrylate
Slurry A (30 vol% solid load) (g)	100	115	2	5	0.56
Slurry B (40 vol% solid load) (g)	100	155	2.5	5	0.85

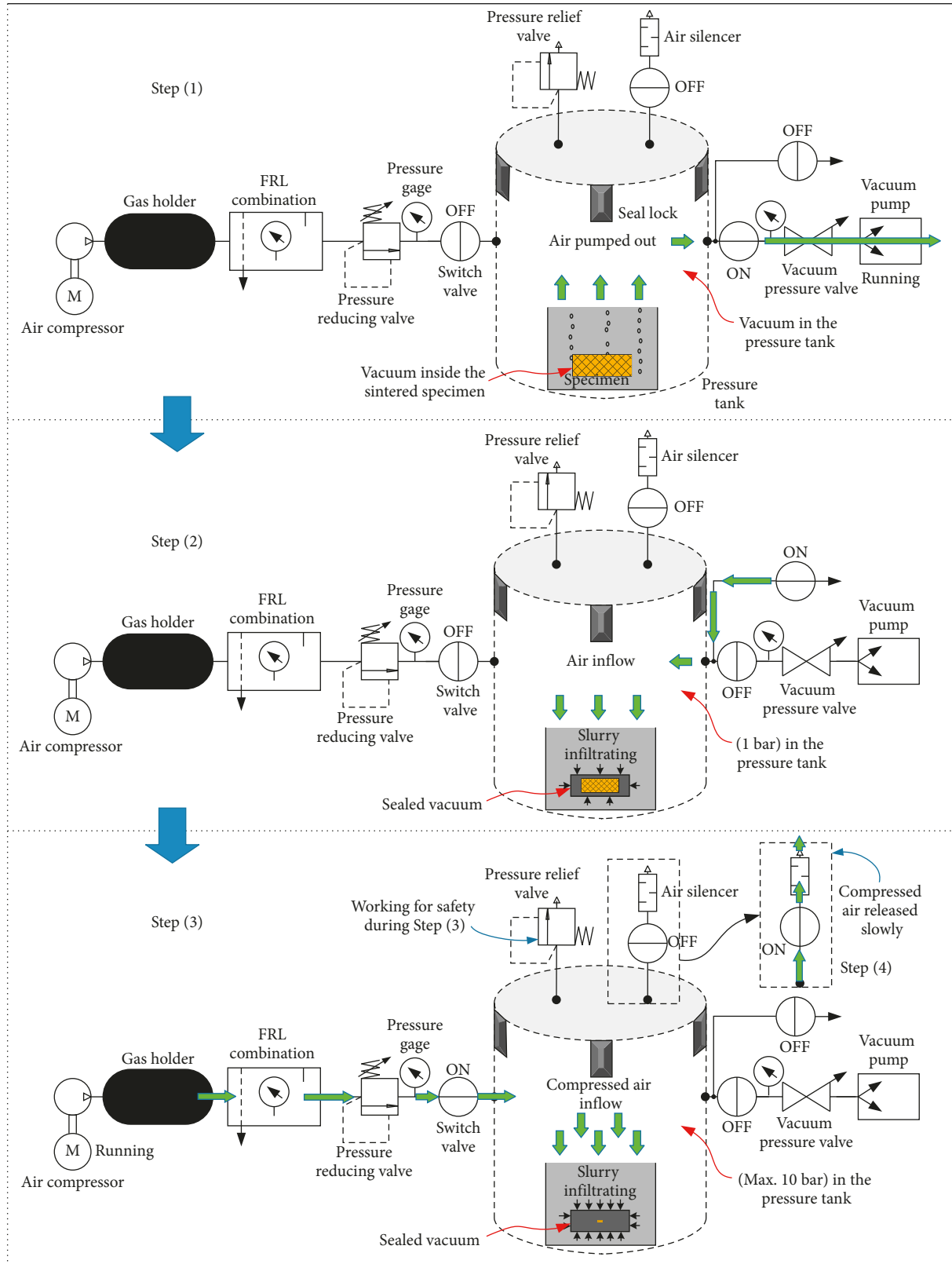


FIGURE 7: Home-made infiltration apparatus and related operations for two working modes.

micro computed tomography (μ CT), and the pore size distributions of the specimens before and after infiltration were evaluated by the mercury pressure method.

2.8. Final Sintering. The temperature schedule in Figure 8 was used for the final sintering in this study. After final sintering, the flexural strength and compressive strength were tested and the microstructures were also characterized, and in comparison with the lengths of printed green specimens, the shrunken lengths of strip-shaped flexural specimens were measured for calculating the total linear shrinkages resulting from the all postprocessing stages.

3. Results and Discussion

3.1. Prepared Material. The microscopic morphology of the prepared powder material is shown in the inset of Figure 9(a). This indicates that the UF binder component basically covers the Al_2O_3 matrix particles, dispensed evenly within the powder material, and reveals only a little agglomeration. The particle size distribution curves shown in Figure 9(b) indicate that each type of powder material has a trimodal size distribution and the abscissa values of particle sizes corresponding to three peaks on the curves are nearly equivalent to the mean sizes of three groups of raw powder component shown in Table 1. Additionally, the three distinguishable regions separated by each particle size distribution curve indicated that their region areas, which represent the actual ratios of the three powder components, have some deviation from the designed ratios shown in Table 1. In summary, from the above discussion, the preparation of powder material in this study, by convenient mechanical blending, could substantially homogenize the raw powder component, but partial deviation still existed. As a result, mechanical tests for the printed green specimens would be necessitated for determining the feasibility of the convenient powder material preparation process to achieve the sufficient bonding strength.

The viscosity, surface tension, and pH value of the prepared printing liquid were 1.09 mPa·s, 61 dyn·cm⁻¹, and 5.1, respectively. This indicates that this weakly acidic aqueous solution free of binder met the jetting requirement of rheological properties by the adopted low-cost desktop piezoelectric printhead and could activate the polycondensation curing reaction of UF binder.

3.2. Printed Green Specimens. The printed green specimens obtained the flexural strength above 6.84 MPa even using Type-A powder which was prepared with only 7.2 wt% ratio of UF binder, as shown in Figure 10. This also indicates that the powder material prepared by mechanical blending was acceptable based on the UF polycondensation curing mechanism in this study. Moreover, the green specimens, printed with Type-B powder containing more UF binder with ratio of 14.3 wt%, obtained the flexural strength up to 8.21 MPa, guaranteeing a good handling performance to specimens in the following processes. It is manifested that the strong bonding of printed specimens is owing to the

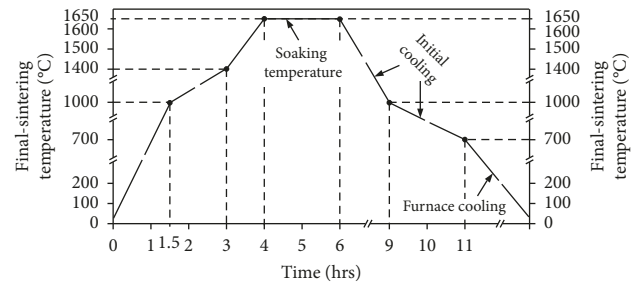


FIGURE 8: Temperature schedule for final sintering process.

curing mechanism by the UF binder. However, the high solubility of powdered UF binder in the aqueous printing liquid also plays an important role. After jetting high-saturation printing liquid onto the powder bed, the fully dissolved UF binder solution could well penetrate into the interstices between the Al_2O_3 matrix particles, even into the areas that had no UF binder homogenized during the preparation of powder material. As shown in Figure 11, the microstructure of the printed green specimens is full of the cured UF binder which wet the Al_2O_3 matrix particles well. Therefore, the sufficient wetting of UF binder solution thorough the Al_2O_3 matrix, as well as the intrinsic high bonding of UF binder, achieves the high flexural strength of the printed parts. It is proved that such a simple material system in this study has great applicability to the ceramic BJP process.

Owing to the flexible process setups of the in-house developed BJP machine system and the related material compositions, the Al_2O_3 green specimens in different experiment groups were printed, with designated initial densities varying within a wide range between 21.7% and 43.9%, as shown in Figure 10. On the one hand, the specimens printed with Type-A powder were realized with higher initial densities than the specimens printed using Type-B powder, since Type-B powder which contained more UF binder could result in stronger “pore-forming” effect after binder pyrolysis, as mentioned above. On the other hand, the initial densities of the printed green specimens were also controllably diversified by setting different powder layer thickness and using different powder layer dispensing methods. With a decreased powder layer thickness, the forces exerted by the roller can be better transmitted into the powder bed which is just dispensed, resulting in denser powder packing by more effective roller compaction. As the thickness of powder layers decreased from 150 μm to 110 μm in the case using CR method, the initial densities of printed green specimens increased from 21.7% to 26.1% when using Type-B powder and from 32.6% to 38.3% when using Type-A powder. The operation of DS method for dispensing one powder layer consists of two round of CR powder layering. The first round is for dispensing powder and giving the initial compaction, and by leveling away a tiny thickness of excess powder layer, the second round layering can conduct the further compaction and fill the surface defects on the surface of powder bed resulting from the first round layering. DS method guaranteed the printed specimen with an initial density up to a high level of 43.9% owing to the

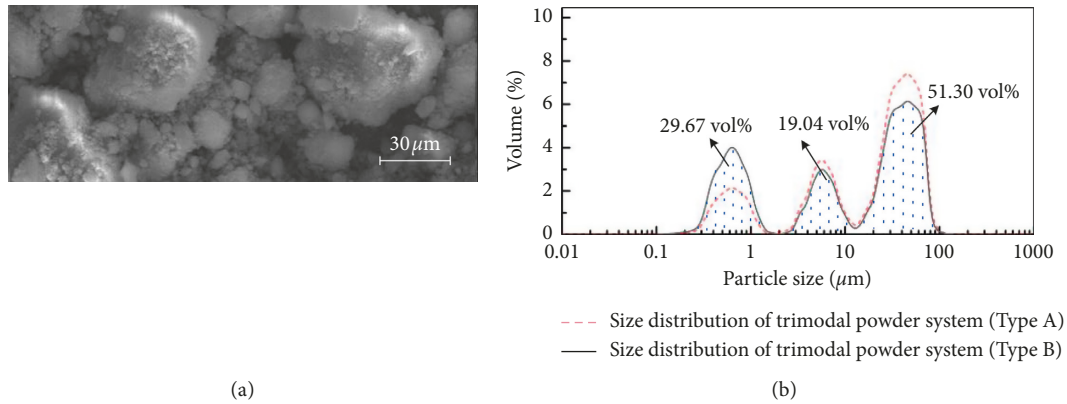


FIGURE 9: Prepared powder material. (a) Microscopic morphology. (b) Size distribution.

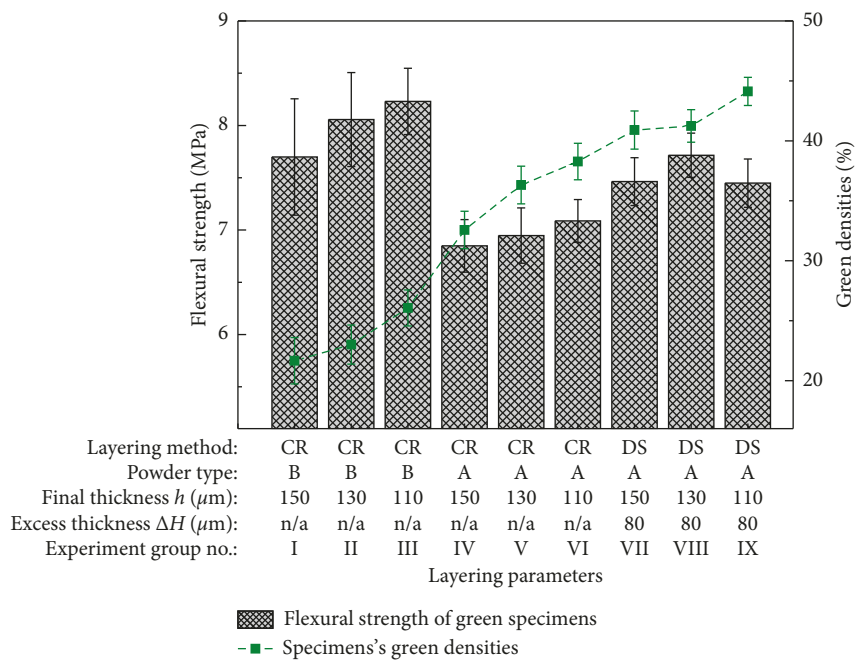


FIGURE 10: Flexural strength and initial green densities of the printed specimens.

double compaction and the reduction of layering defects, whereas the printed specimens using the CR method only reached about 38.3% by using the same layering parameters of Type-A powder and the layer thickness of 110 μm . In general, this study presents a flexible BJP solution for printing ceramic green specimens with adjustable structures and high strength, which also benefit the following research on the influences of parts' structural characteristics on the postprocessing.

3.3. Debinded and Presintered Specimens. Compared with the microstructures of printed specimens in Figure 11, the debinded structure in Figure 12(a) appears remarkably loose and porous due to the thermal decomposition of UF component. At this stage, the specimens reveal no bonding except for a few undecomposable binder residues existing between the Al_2O_3 matrix particles. Consequently, the

debinding was followed with the presintering which guaranteed the adequate mechanical strength to the debinded specimens for retaining their structural integrities during the postprocessing, especially during the process of pressure infiltration of ceramic slurry. After presintering, the microscopic morphology in Figure 12(b) shows that Al_2O_3 grains within the debinded ceramic matrix begin to grow, and then the adjacent Al_2O_3 particles gradually migrate to form the necks. The adhesion of the particle necks gives the presintered specimens the preliminary mechanical strength to withstand the working pressure in the following ceramic slurry infiltration. Meanwhile, the interconnected necks also form the network structures as the infiltration paths within the presintered specimens. The XRD analysis in Figure 12(c) proves that the diffraction patterns for the ground powder from debinded and presintered specimens are generally consistent with those of the raw alumina powder. As a result, the debinded and presintered specimens are determined as a

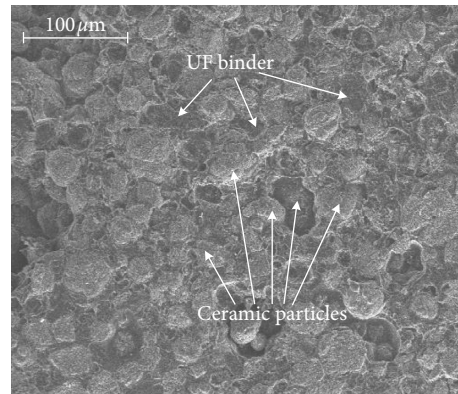
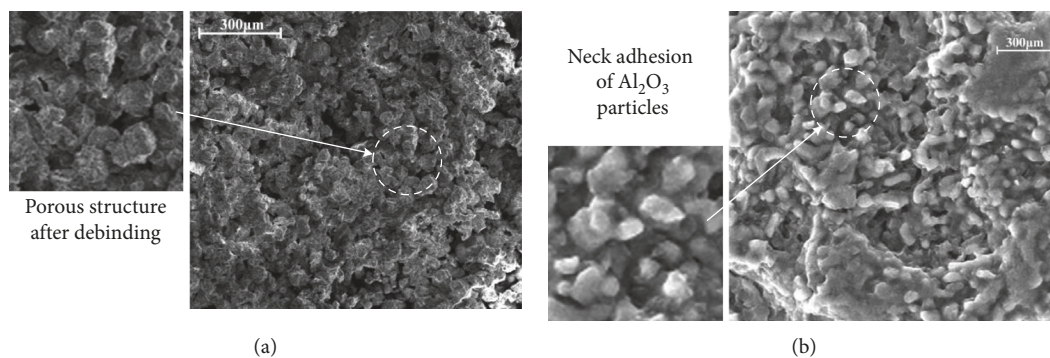
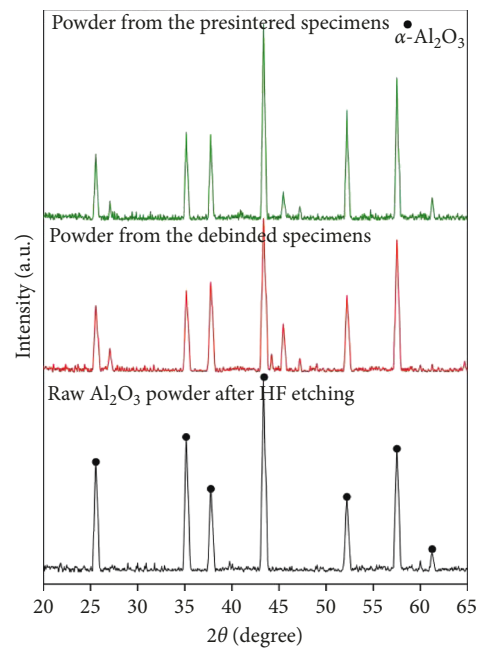


FIGURE 11: SEM image of the printed green specimens' microstructures cured by UF binder.



(a)

(b)



(c)

FIGURE 12: (a) Specimens' microstructures after debinding. (b) Specimens' microstructures after presintering. (c) XRD results for debinded specimens, presintered specimens, and the as-received raw Al_2O_3 powder.

structure form of $\alpha\text{-Al}_2\text{O}_3$ matrix, which facilitates the part densification in postprocessing.

It is shown in Figure 13(a) that the decrease of printed specimens' initial densities restricts the density increment

strengthened by the presintering. As the initial densities of the printed green specimens decreased from 43.9% to 21.7%, the densities increment therewith reduced from 11.04% to 0.83%. Consequently, the printed specimens with lower

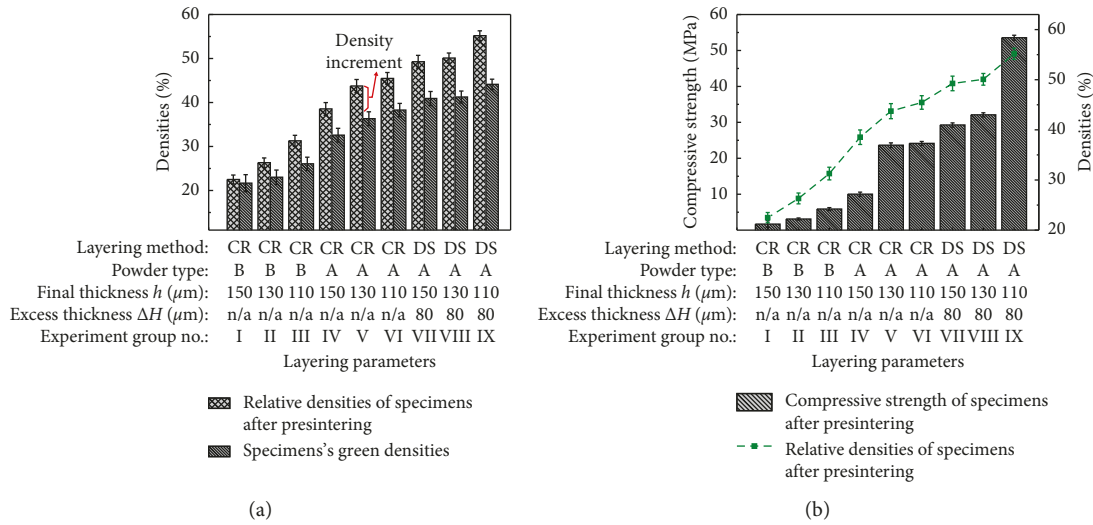


FIGURE 13: (a) Variations of presintered specimens' densities along with their initial densities. (b) Variations of presintered specimens' compressive strength along with their densities after presintering.

initial densities would also obtain the lower densities after presintering. Moreover, as shown in Figure 13(b), the poor densification after presintering also limits the compressive strength of the presintered specimens. The specimen in Group I had the lowest initial green density of 21.7%. After presintering, its density was slightly increased to 22.5% and the compressive strength was only 1.6 MPa which even could not withstand the working pressure during the follow-up infiltration process. In contrast, the green specimen in Group IX had the highest initial densities of 43.9% due to DS method dispensing powder layers. After presintering, the density was increased to 54.9% and the corresponding compressive strength was up to 53.5 MPa. These results explain that Al_2O_3 particles within the loose specimens have large spacing with each other, the grain growth by the sintering energy is thereby insufficient, and as a result, the neck adhesion between the particles is significantly reduced, weakening the densification and the structural strength of the presintered specimens.

3.4. Mechanism of Ceramic Slurry Infiltration. The compressive strength of the presintered specimens in Groups II, III, IV, VI, VI, and IX was adequate for withstanding the working pressure in the ceramic slurry infiltration and was used for the following investigation on the influences of the infiltration process by the specimens' structural characteristics. The pore size distribution of above specimens before and after infiltration was tested. As the example result of specimen in Group VI shown in Figure 14, it is found that the relative volume of the pores (i.e., porosity) for the size below about $1.13\ \mu\text{m}$ was increased through infiltration, whereas the larger pores reduced dramatically after infiltration. This gives an assumption that the ceramic slurry only effectively penetrates the large-scale pores within the presintered specimens. Inspired by this assumption, the results of porosities (for the pore size over $1.1\ \mu\text{m}$) for specimens before infiltration are listed as in Table 5; in

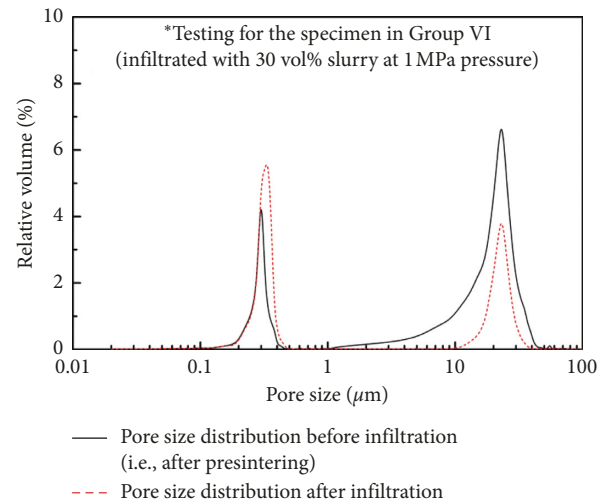


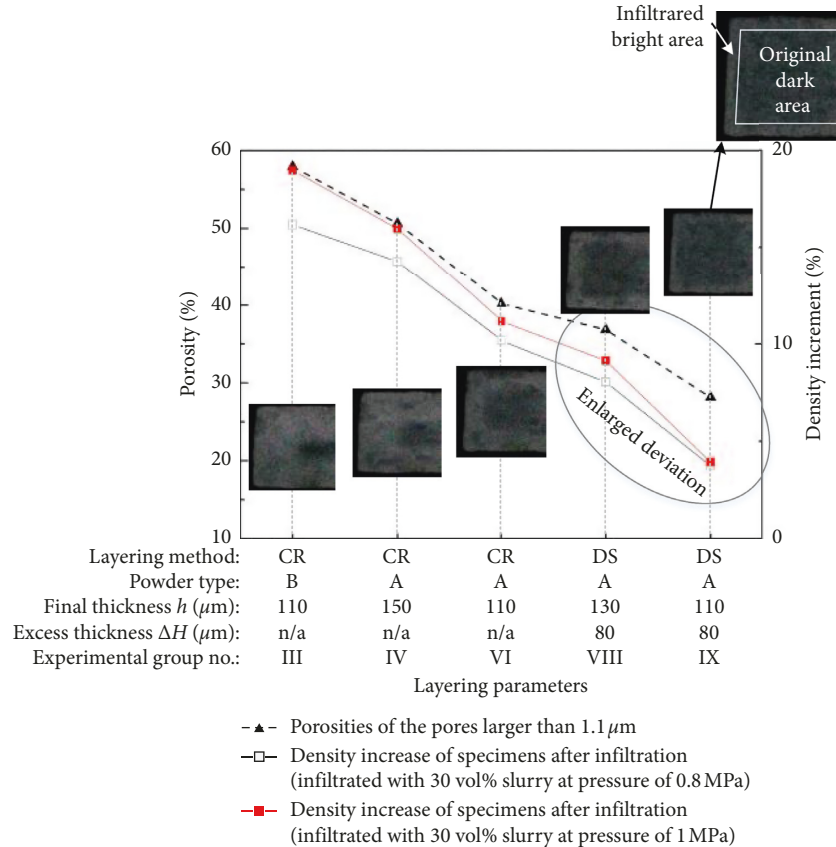
FIGURE 14: Pore size distribution before and after infiltration (an example of the specimens in Group VI).

addition, the relationship between these porosity results and the corresponding density increment of these specimens through infiltration depicted in Figure 15 shows that the tendency of the density increment between the experiment groups is similar to that for the porosities. This indicates that the density increment induced by infiltration, to a large extent, is determined by the existing number of large-scale pores within the specimens before infiltration, proving the above assumption that the slurry only effectively penetrates the large-scale pores.

The μCT insets in Figure 15 exhibit the conditions of penetrating 30 vol% ceramic slurry at 1 MPa into the presintered specimens with different densities corresponding to different groups. Note that the infiltrated areas would turn to be brighter, whereas the original porous structures appear dark. It is found from the μCT results that the penetration path of the slurry is isotopically diffused into the interior of

TABLE 5: Porosities of large-scale pores ($\geq 1.1 \mu\text{m}$) within presintered specimens before infiltration.

Group no.	Densities after presintering (%)	Porosities ($\geq 1.1 \mu\text{m}$ pores) (%)
III	31.1	57.95
IV	38.1	50.63
VI	45.2	40.21
VIII	49.5	36.82
IX	54.9	28.11

FIGURE 15: Relationship between the specimens' density increments induced by infiltration and the porosities of large pores ($\geq 1.1 \mu\text{m}$) within presintered specimens.

the printed specimens, and the infiltrated areas get narrower with the increase of specimen densities before infiltration. Like the presintered specimens with high densities in Groups VIII and IX, infiltration stopped at a shallow depth. As infiltration stopped early, the ceramic slurry even had no access to the macropores inside the specimens. As a result, the infiltration effects for these high-density specimens were further weakened. This explains for Figure 15 that the deviation, between the curve of density increment and the curve of macropore porosity curve, is enlarged for the high-density specimens in Groups VIII and IX.

As shown in Figure 16, whether using 30 vol% or 40 vol% slurry, the higher infiltration pressure results in the larger density increment for the presintered specimens in each experiment group. Figure 16(a) further shows that after infiltration with 30 vol% slurry at any infiltration pressure, the resultant density increment was larger if the specimen densities before infiltration was lower. This is consistent with

the above conclusion that slurry only effectively penetrates the large-scale pores. As shown in Table 5, the lower density before infiltration indicates more large-scale pores existing within the presintered specimens, which facilitates the infiltration and realizes larger density increment. These results can also be interpreted as below. The main factors for hindering the infiltration are the frictional resistance of slurry and the residual air pressure continuously compressed in the microchannel. The specimens with the lower densities contain the relatively larger infiltration channel; therefore, the drag coefficient of the slurry and the compression rate of the residual are smaller, benefiting the infiltration process. In contrast, the internal channels within dense specimens are smaller and prone to absorb the slurry moisture due to the capillary action, making the slurry more viscous and severely restricting the infiltration process.

Comparing Figures 16(a) with 16(b), the ceramic slurry with higher solid loads of 40 vol% realizes larger density

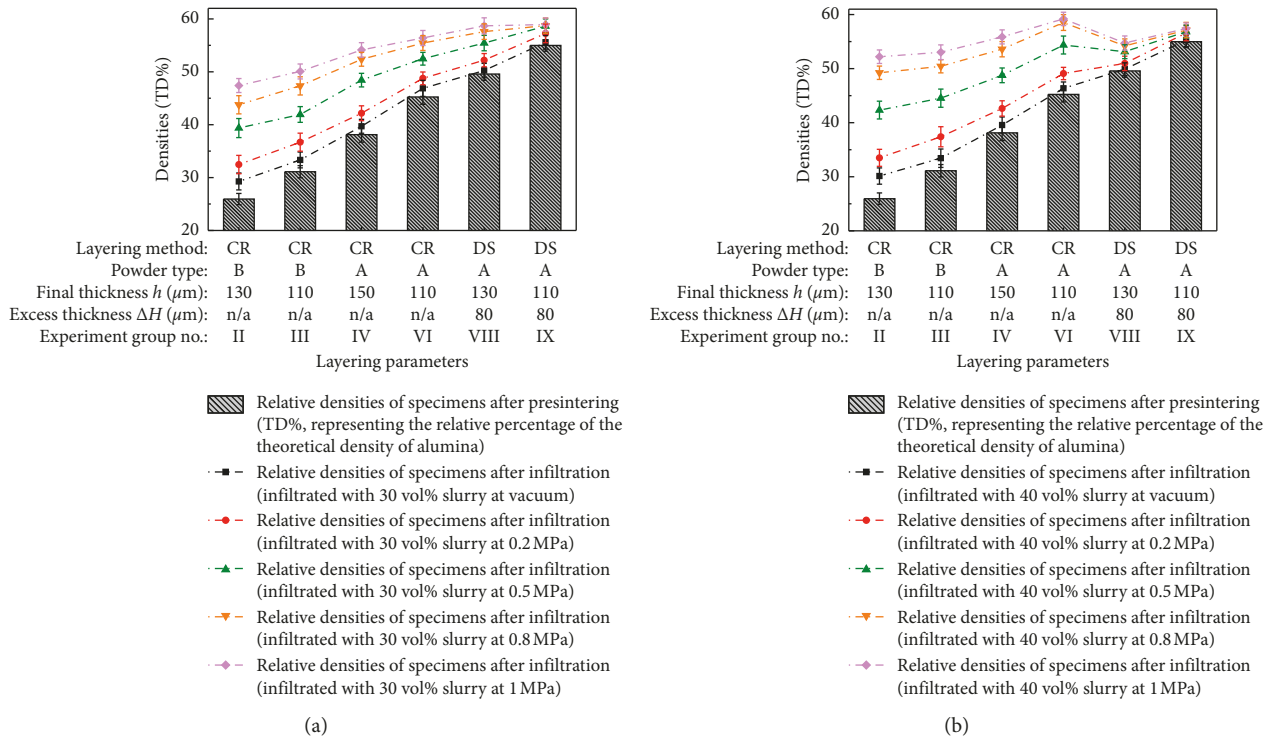


FIGURE 16: Density increment of the specimens by various infiltration parameters (including different solid loads in slurries and different infiltration pressures). (a) Infiltrating with 30 vol% solid-load slurry. (b) Infiltrating with 40 vol% solid-load slurry.

increments after infiltration than the case using 30 vol% ceramic slurry for the specimens in Groups II, III, IV, and VI. However, for the high-density specimens in Groups VIII and IX, the density increments by using 40 vol% slurry are contrarily smaller than the case using 30 vol% ceramic slurry. This explains that the smaller internal channel in the high-density specimens is more sensitive to the slurry and the increase of viscosity by higher solid loadings would weaken the infiltration. As a result, after infiltrating using 40 vol% ceramic slurry at 1 MPa, the density of the infiltrated specimen in Group VI reached 59.2% which was higher than the infiltrated specimens in Group VIII and IX (54.7% and 57.4%, respectively). However, noting that, before infiltration, the density of specimens in Group VI was 45.2%, lower than those for the specimens in Group VIII and IX (49.6% and 54.9%, respectively). This indicates that the presintered structures have significant influence on the infiltration effect. It is inspired by the above analysis that the future work can focus on optimizing the presintering temperature schedule for the printed parts with high green densities like the specimens in Groups VIII and IX to retain more macropores in the presintered parts while ensuring the adequate part strength. Considering infiltration favorable for macropores, the better infiltration effects for the high-density green parts can be therewith achieved, and also, the potential of the above BJP solution capable of producing high-density specimens can be fully realized.

3.5. Performances of the Final-Sintered Specimens. Figures 17(a) and 17(b) show the densification effects of the above infiltrated specimens after final sintering. Whether

using 30 vol% or 40 vol% Al_2O_3 slurry, the infiltrated specimens with denser structures would have the higher densities after final sintering. As mentioned above, the specimen in Group VI, with the initial green density (38.3%) lower than those for the specimens in Group VIII (41.1%) and Group IX (44.1%), would contrarily obtain higher density after infiltration using 40 vol% slurry at 1 MPa working pressure because of having more macropores capable of effective slurry infiltration. As a result, after final sintering, the specimen in Group VI still realized the higher level of densification (73.2%) than the specimens in Group VIII (67.2%) and Group IX (70.1%), as shown in Figure 17(b). This tells that the Al_2O_3 slurry, well penetrating into Group VI specimens, offered the additional promoting effect on the final sintering by virtue of high sintering kinetics deriving from the surface activity of submicron Al_2O_3 particles. Therefore, it is indicated that the previous step of infiltration process played a key role in the integrated postprocessing procedure adopted in this study.

According to the measured length of the long-strip specimens after printing and after final sintering, the total linear shrinkages resulting from the whole integrated postprocessing procedure were calculated as shown in Figure 18. As the densities of the final-sintered specimens in Groups II, III, IV, and VI increased, the volume shrinkages induced by postprocessing were consequently increased, resulting in the larger linear shrinkages. In addition, the density of the final-sintered specimen in Group VI was comparable, even higher than that of the final-sintered specimens in Groups VIII and IX in the case of infiltration with 40 vol% slurry; furthermore, the initial density of the

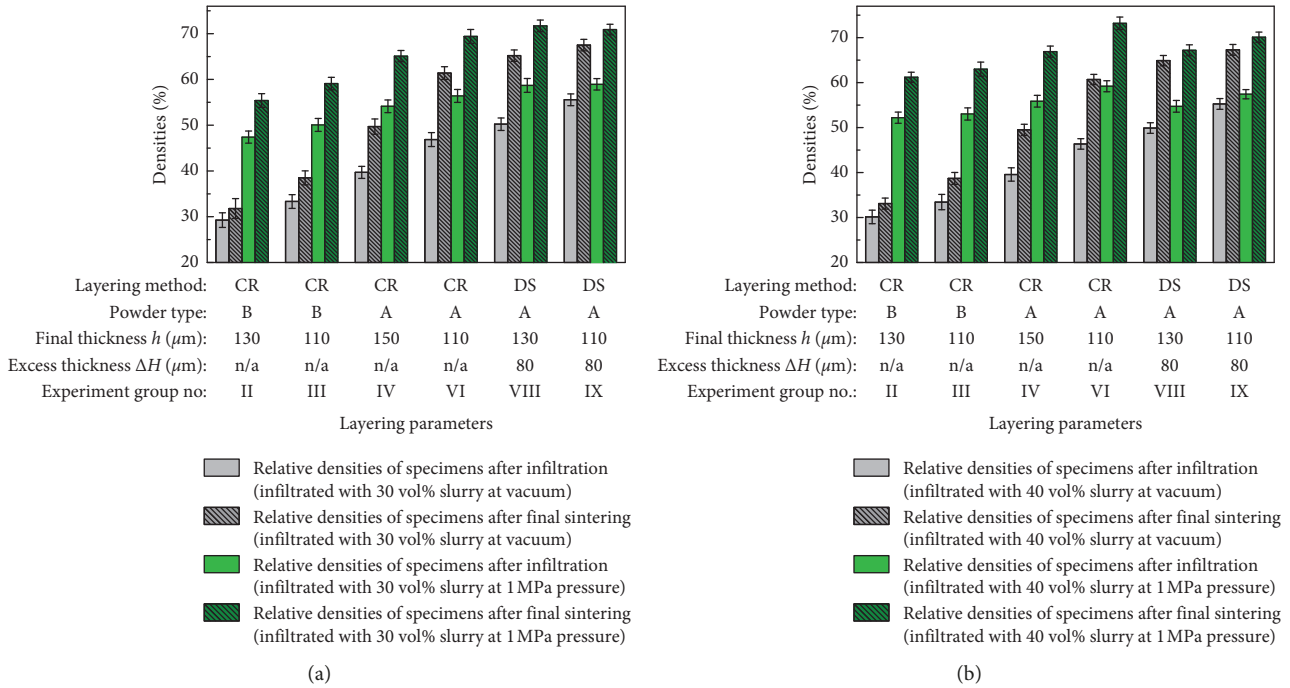


FIGURE 17: Variation of infiltrated specimens' densities through final sintering. (a) Specimens infiltrated with 30 vol% slurry. (b) Specimens infiltrated with 40 vol% slurry.

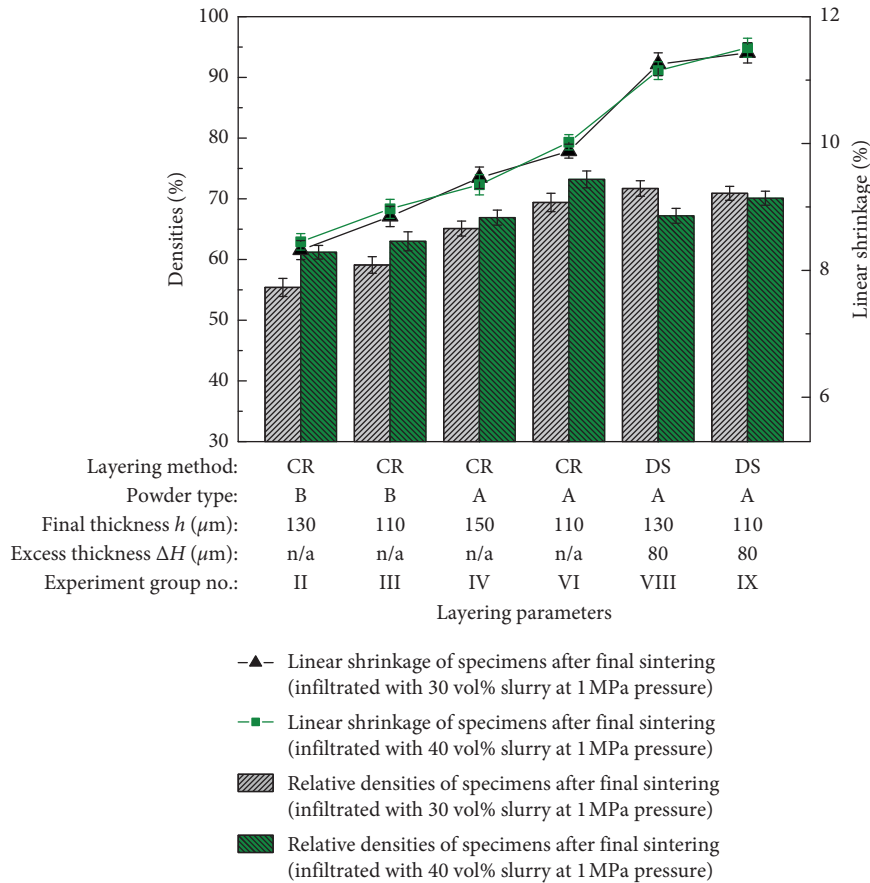


FIGURE 18: Variations of final-sintered specimens' linear shrinkages along with their final densities.

printed green specimen in Group VI was smaller than those in Groups VIII and IX as mentioned above. That is to say, the specimen in Group VI realized a larger density increment than the specimens in Group VIII and IX during the whole integrated postprocessing procedure and should reveal more volume shrinkages. However, the linear shrinkage of the specimen of Group VI was 9.88%, and the specimens of Groups VIII and IX proved the higher linear shrinkages on the contrary, which were 11.25% and 11.43%, respectively. The reduction of the linear shrinkages of the specimen in Group VI can be explained by the benefit from slurry infiltration. On the one hand, the ceramic compositions infiltrated into the specimen in Group VI directly improved the densification, and the resultant density increment was not related to the volume shrinkage. On the other hand, the infiltration effects for the specimens in Groups VIII and IX were weak, and accordingly, the density increment during the whole postprocessing procedure was almost induced by different stages of sintering, i.e., by the volume shrinkages. As a result, the specimen in Group VI with great infiltration effect obtained the smaller linear shrinkage than those less infiltrated in Groups VIII and IX, demonstrating the feasibility of the slurry infiltration for restricting the part shrinkage during postprocessing.

After final sintering, the flexural strength and compressive strength of the specimens were measured as shown in Figures 19(a) and 19(b). When infiltrating with any type of slurry, the flexural and compressive strength of the final-sintered specimens in Groups II, III, IV, and VI improved with the increase of their final densities. In addition, the density of the final-sintered specimen in Group VI was comparable, even higher in comparison with that of the final-sintered specimens in Groups VIII and IX in the case of infiltration with 40 vol% slurry; however, the final flexural and compressive strength of the specimen in Group VI was significantly smaller than those in Groups VIII and IX: the final flexural strength in Group VI was 43.15 MPa while the ones in Groups VIII and IX were 59.58 MPa and 63.22 MPa, respectively; the final compressive strength in Group VI was 331.17 MPa while the ones in Groups VIII and IX were 436.89 MPa and 450.18 MPa, respectively. Note that the specimens in Groups VIII and IX were provided with high green densities through BJP process using the DS powder-layering method, and this might account for their high mechanical strength after final sintering. The initial dense structure of the green specimens indicates the small spacing between the original Al_2O_3 particles, which is beneficial to the particle migration during the process of sintering. As a result, the adhesion of necks between the particles are easily generated after sintering, resulting in the more stable ceramic skeleton. The skeleton is mainly composed of the Al_2O_3 matrix powder from the original powder material, which can better support the whole structure. In addition, the interior of the high-density specimens in Groups VIII and IX has no slurry penetrated during the infiltration process, so the remaining internal porous structure can also buffer the fracture cracks, thereby improving the mechanical properties.

As mentioned above, only surface areas in the high-density specimens were infiltrated with the ceramic slurry. For identifying the effects of ceramic slurry infiltration on these high-density specimens, a few printed green specimens were additionally selected from Groups VIII and IX, respectively, marked as reference specimens A and B. These reference specimens in this study were postprocessed just by one-step sintering for performance comparison with the corresponding specimens in Group VIII and IX strengthened by integrated postprocessing procedure. As shown in Table 6, even postprocessed just by sintering, the reference specimens A and B, with high initial green densities, would have great densification and mechanical performances, comparable to the integrated postprocessing specimens in Groups VIII and IX. This indicates that due to high-dense structures of initial green parts realized by BJP solution in this study, postprocessing procedure can be simplified for high-strength ceramic products. On the other hand, it is found from Table 6 that the final surface roughness and hardness of the specimens in Groups VIII and IX are significantly superior to those of the corresponding reference specimens just postprocessed by sintering, demonstrating the surface strengthening effects by the slurry infiltration process.

4. Conclusions and Future Work

- (1) In this study, the BJP solution, based on the polycondensation curing mechanism of powdered UF resin, printed Al_2O_3 green specimens with high densities and strength. The initial structures of the green specimens could be controlled through the flexible process setups of the self-developed BJP system and the easily prepared material. The flexural strength of the green specimens was above 6.84 MPa and the initial densities of the green specimens can be regulated between 21.7% and 43.9%. Even simply postprocessed by sintering, the high-dense green specimens with 43.9% initial density could achieve the final densities, flexural strength, and compressive strength of above 70%, 62.6 MPa, and 435.3 MPa, respectively. This suggests that the BJP solution in this study is convenient and suitable to bond various ceramic powders to form the high-density green parts, which facilitates high-performance ceramic AM by simplified postprocessing under atmospheric pressure.
- (2) An integrated postprocessing procedure, including presintering, ceramic slurry infiltration, and final sintering, was performed on a series of green specimens with varied structures. The influences of green specimens' structural characteristics on the postprocessing were evaluated. It is demonstrated in this study that the submicron Al_2O_3 particles are prone to infiltrate the large-scale pores (above 1.1 μm) within the presintered specimens and very beneficial to strengthen the printed green specimens expect for the ones with initial densities over 40%. Infiltrated by a self-made convenient infiltration

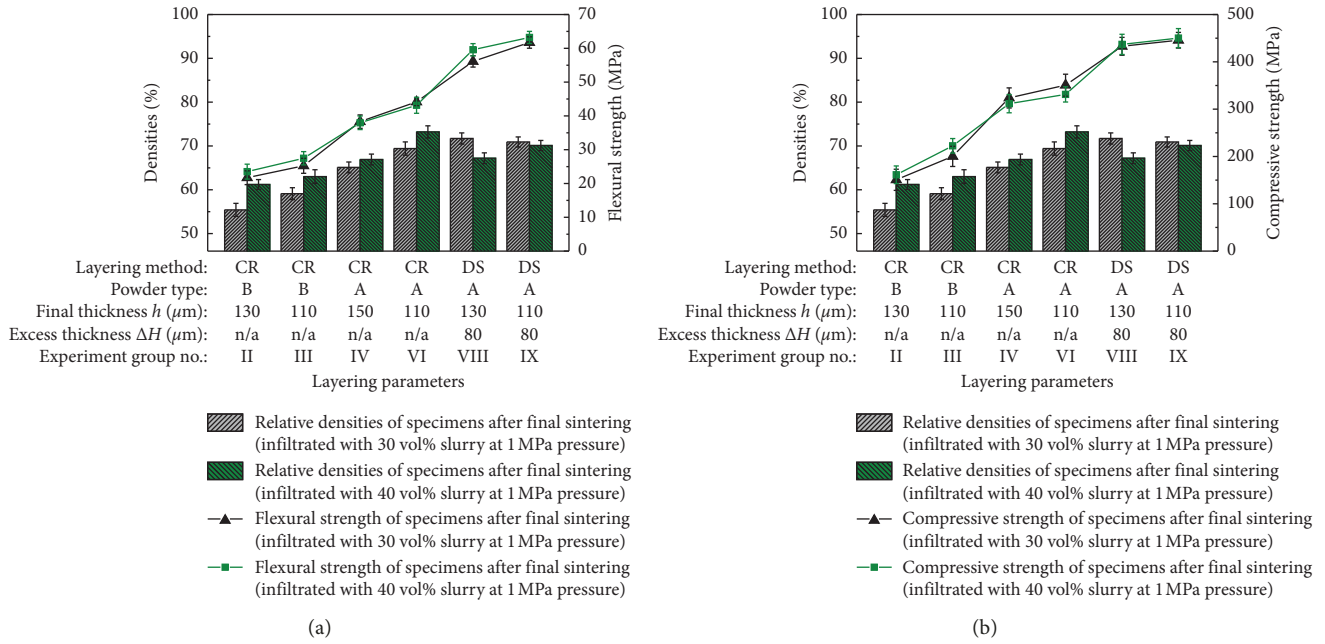


FIGURE 19: Variations of final-sintered specimens' mechanical strength along with their final densities. (a) Flexural strength. (b) Compressive strength.

TABLE 6: Comparison of final part performances between the integrated processing specimens in Groups VIII and IX and the corresponding reference specimens A and B postprocessed just by sintering.

Item for part performance	Specimen in group VIII ¹	Ref. specimen A	Specimen in group IX ¹	Ref. specimen B
Relative densities (%)	67.2 ± 1.22	66.4 ± 0.97	70.1 ± 1.15	67.8 ± 1.07
Flexural strength (MPa)	59.6 ± 1.81	59.9 ± 1.36	63.2 ± 1.79	62.6 ± 1.47
Compressive strength (MPa)	436.9 ± 21.33	431.6 ± 18.71	450.2 ± 20.11	435.3 ± 16.35
Surface roughness R_a (μm)	9.55 ± 0.43	16.73 ± 1.23	9.73 ± 0.56	16.01 ± 0.85
Vickers hardness (under 5 kgf, GPa)	4.47 ± 0.18	1.03 ± 0.29	4.58 ± 0.15	1.28 ± 0.39

¹The specimens of Group VIII (IX) were infiltrated with 40 vol% slurry at 1 MPa pressure during the integrated postprocessing procedure.

apparatus at only 1 MPa applied pressure, the densities of specimens could be increased by 34% after final sintering, from the initial densities between 25% and 30%. The green specimens with the initial density about 35% obtained the strongest improvement in densification after the postprocessing. The final density reached 73.2%; however, the flexural strength and compressive strength were only 43.2 MPa and 331.2 MPa, respectively. In comparison, the green specimens with higher initial densities (about 43%) obtained a smaller final density (70.1%) due to the pore infiltration effect, but they obtained remarkably higher final flexural and compressive strength of 63.2 MPa and 450.2 MPa, respectively. These results indicated that the original high-dense ceramic matrix formed through above BJP solution is very beneficial to the specimens' final mechanical properties. Moreover, the infiltrated ceramic slurry has the remarkable effect on limiting the part shrinkage during the sintering.

(3) The green specimens, formed by above BJP solution using the DS powder-layering method and low ratio of binder component, achieved the high initial density of 43%. However, the slurry infiltration into the high-density green specimens was restricted at the shallow surfaces. Compared with the reference specimens not infiltrated, the shallow-infiltrated specimen exhibited the remarkably better surface roughness and hardness, but the comparable mechanical strength due to the absence of infiltration inner the structure. It is inspired that the presintering process should be further designed in the future work to remain as many large-scale pores as possible within the presintered parts and meanwhile ensure their adequate strength. In this way, the effect of the ceramic-slurry infiltration for the high-density green parts can be improved and these parts' structural advantages can be fully exploited during the postprocessing strengthening.

Data Availability

The data used to support the findings of this study are available from the corresponding author upon request.

Conflicts of Interest

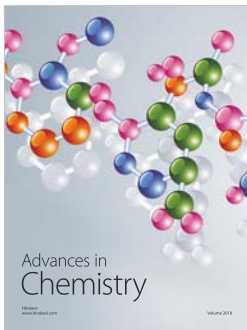
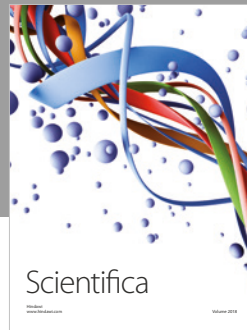
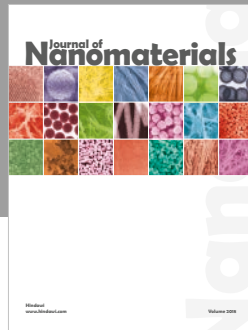
The authors declare that there are no conflicts of interest regarding the publication of this paper.

Acknowledgments

This work was financially supported by the Natural Science Foundation of China (51605193), Natural Science Foundation of Jiangsu Province, China (BK20160181), Fundamental Research Funds for the Central Universities (JUSRP11716), and Open Research Fund of Jiangsu Key Laboratory of Advanced Food Manufacturing Equipment & Technology (FM-201607). Besides, this study was also partially supported by the research project (FMZ2018Y2) from the Jiangsu Key Laboratory of Advanced Food Manufacturing Equipment and Technology.

References

- [1] Y. Hu and W. Cong, "A review on laser deposition-additive manufacturing of ceramics and ceramic reinforced metal matrix composites," *Ceramics International*, vol. 44, no. 17, pp. 20599–20612, 2018.
- [2] H.-H. Tang, M.-L. Chiu, and H.-C. Yen, "Slurry-based selective laser sintering of polymer-coated ceramic powders to fabricate high strength alumina parts," *Journal of the European Ceramic Society*, vol. 31, no. 8, pp. 1383–1388, 2011.
- [3] W. Gao, Y. Zhang, D. Ramanujan et al., "The status, challenges, and future of additive manufacturing in engineering," *Computer-Aided Design*, vol. 69, pp. 65–89, 2015.
- [4] K. S. Prakash, T. Nancharai, and V. V. S. Rao, "Additive manufacturing techniques in manufacturing-an overview," *Materials Today: Proceedings*, vol. 5, no. 2, pp. 3873–3882, 2018.
- [5] D. Bourell, J. P. Kruth, M. Leu et al., "Materials for additive manufacturing," *CIRP Annals*, vol. 66, no. 2, pp. 659–681, 2017.
- [6] M. Schwentenwein and J. Homa, "Additive manufacturing of dense alumina ceramics," *International Journal of Applied Ceramic Technology*, vol. 12, no. 1, pp. 1–7, 2015.
- [7] X. Lv, F. Ye, L. Cheng, S. Fan, and Y. Liu, "Binder jetting of ceramics: powders, binders, printing parameters, equipment, and post-treatment," *Ceramics International*, vol. 45, no. 10, pp. 12609–12624, 2019.
- [8] I. Götschel, B. Gutbrod, N. Travitzky, A. Roosen, and P. Greil, "Processing of preceramic paper and ceramic green tape derived multilayer structures," *Advances in Applied Ceramics*, vol. 112, no. 6, pp. 358–365, 2013.
- [9] S. Mamatha, P. Biswas, P. Ramavath, D. Das, and R. Johnson, "3D printing of complex shaped alumina parts," *Ceramics International*, vol. 44, no. 16, pp. 19278–19281, 2018.
- [10] T. Chartier, A. Badev, Y. Abouliatim, P. Lebaudy, and L. Lecamp, "Stereolithography process: influence of the rheology of silica suspensions and of the medium on polymerization kinetics—cured depth and width," *Journal of the European Ceramic Society*, vol. 32, no. 8, pp. 1625–1634, 2012.
- [11] K. Shahzad, J. Deckers, Z. Zhang, J.-P. Kruth, and J. Vleugels, "Additive manufacturing of zirconia parts by indirect selective laser sintering," *Journal of the European Ceramic Society*, vol. 34, no. 1, pp. 81–89, 2014.
- [12] J. P. Deckers, K. Shahzad, L. Cardon, M. Rombouts, J. Vleugels, and J.-P. Kruth, "Shaping ceramics through indirect selective laser sintering," *Rapid Prototyping Journal*, vol. 22, no. 3, pp. 544–558, 2016.
- [13] W. Du, X. Ren, C. Ma, and Z. Pei, "Ceramic binder jetting additive manufacturing: particle coating for increasing powder sinterability and part strength," *Materials Letters*, vol. 234, pp. 327–330, 2019.
- [14] N. Travitzky, A. Bonet, B. Dermeik et al., "Additive manufacturing of ceramic-based materials," *Advanced Engineering Materials*, vol. 16, no. 6, pp. 729–754, 2014.
- [15] E. Feilden, D. Glymond, E. Saiz, and L. Vandeperre, "High temperature strength of an ultra high temperature ceramic produced by additive manufacturing," *Ceramics International*, vol. 45, no. 15, pp. 18210–18214, 2019.
- [16] K. Subramanian, N. Vail, J. Barlow, and H. Marcus, "Selective laser sintering of alumina with polymer binders," *Rapid Prototyping Journal*, vol. 1, no. 2, pp. 24–35, 1995.
- [17] W. Zhang, R. Melcher, N. Travitzky, R. K. Bordia, and P. Greil, "Three-dimensional printing of complex-shaped alumina/glass composites," *Advanced Engineering Materials*, vol. 11, no. 12, pp. 1039–1043, 2009.
- [18] B. Utela, D. Storti, R. Anderson, and M. Ganter, "A review of process development steps for new material systems in three dimensional printing (3DP)," *Journal of Manufacturing Processes*, vol. 10, no. 2, pp. 96–104, 2008.
- [19] K. Liu, Y. Shi, W. He, C. Li, Q. Wei, and J. Liu, "Densification of alumina components via indirect selective laser sintering combined with isostatic pressing," *The International Journal of Advanced Manufacturing Technology*, vol. 67, no. 9–12, pp. 2511–2519, 2013.
- [20] S. Maleksaeedi, H. Eng, F. E. Wiria, T. M. H. Ha, and Z. He, "Property enhancement of 3D-printed alumina ceramics using vacuum infiltration," *Journal of Materials Processing Technology*, vol. 214, no. 7, pp. 1301–1306, 2014.
- [21] J. Deckers, J.-P. Kruth, K. Shahzad, and J. Vleugels, "Density improvement of alumina parts produced through selective laser sintering of alumina-polyamide composite powder," *CIRP Annals*, vol. 61, no. 1, pp. 211–214, 2012.
- [22] M. Stumpf, N. Travitzky, P. Greil, and T. Fey, "Sol-gel infiltration of complex cellular indirect 3D printed alumina," *Journal of the European Ceramic Society*, vol. 38, no. 10, pp. 3603–3609, 2018.
- [23] K. Shahzad, J. Deckers, J.-P. Kruth, and J. Vleugels, "Additive manufacturing of alumina parts by indirect selective laser sintering and post processing," *Journal of Materials Processing Technology*, vol. 213, no. 9, pp. 1484–1494, 2013.
- [24] M. Dunky, "Urea-formaldehyde (UF) adhesive resins for wood," *International Journal of Adhesion and Adhesives*, vol. 18, no. 2, pp. 95–107, 1998.
- [25] S. Cao, Y. Qiu, X.-F. Wei, and H.-H. Zhang, "Experimental and theoretical investigation on ultra-thin powder layering in three dimensional printing (3DP) by a novel double-smoothing mechanism," *Journal of Materials Processing Technology*, vol. 220, pp. 231–242, 2015.
- [26] L. Palmqvist, O. Lyckfeldt, E. Carlström, P. Davoust, A. Kauppi, and K. Holmberg, "Dispersion mechanisms in aqueous alumina suspensions at high solids loadings," *Colloids and Surfaces A: Physicochemical and Engineering Aspects*, vol. 274, no. 1–3, pp. 100–109, 2006.



Hindawi
Submit your manuscripts at
www.hindawi.com

